Chapter 6

Development of a Photovoltaic-Wind Hybrid Energy Conversion System

6.1 Introduction

After exploring the design and development of the power converters for efficiently extracting solar power from the PV generation and wind power from the WECS, the end goal of the development of a HECS is achieved and is presented in this chapter. [14–17] have explored the hybrid cogeneration from solar and wind power systems, but the focus was on the operational modes and control of the power flow. In this chapter, the other aspect of improving the performance of the PV generation and WECS is explored as well. The results obtained from the Matlab/Simulink version 10.2 are presented and discussed in here as well.

For performing the MPPT on PV panels, the input-current ripple-free DC-DC converter presented in Chapter 3 is used in developing this HECS as all the aspects of higher voltage gain and ripple-free operation is achieved through this converter. The converter presented in Chapter-2 has lower voltage stress than the converter presented in chapter 3, but the presence of current ripple at the output and relatively lower voltage gain makes it less preferred.

In the case of the WECS, the topology presented in chapter 4 is preferred over the topology presented in chapter 3, as it has a lower operating frequency, lower device count, and is more compatible with PMSG fed systems. The elimination of gearbox, i.e., direct-drive possibility, makes it more lucrative. Furthermore, the adoption of the TSR-following

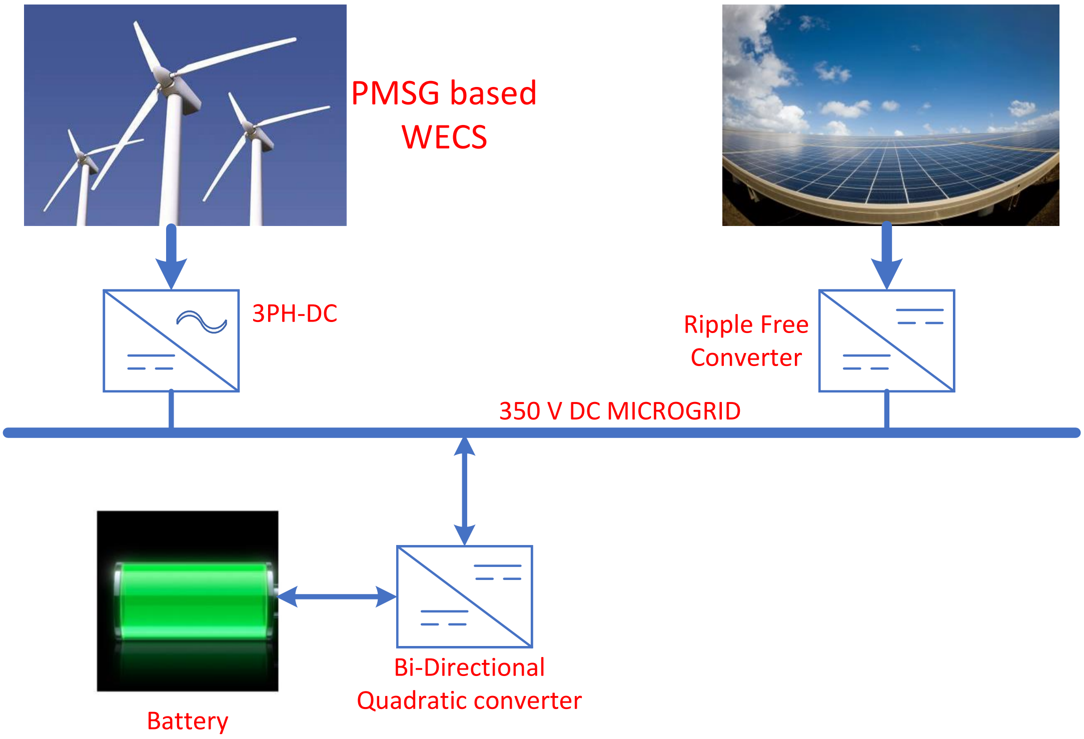

Figure 6.1: Schematic of the system with battery.

MPPT technique is deemed more apt for turbines with fixed blade pitch. In low power highly-distributed WECS, the blade pitch is kept constant for simplicity, low cost and less liability.

6.2 HECS Feeding a DC Microgrid with BESS

The schematic diagram of the developed HECS with BESS-based microgrid control is shown in Figure 6.1. The power flow from and to the DC microgrid is controlled through a bidirectional DC-DC converter through a BESS. For this purpose, a non-isolated quadratic gain bidirectional converter is used. The topology of the bidirectional converter is shown in Figure 6.2.

6.2.1 PV generation

The operation and performance of the PV and WECS generation systems are unchanged, as presented in chapters 3 and 5. The ability of the quadratic gain bi-directional converter is tested here when there is a large change in the operating point of the solar and wind

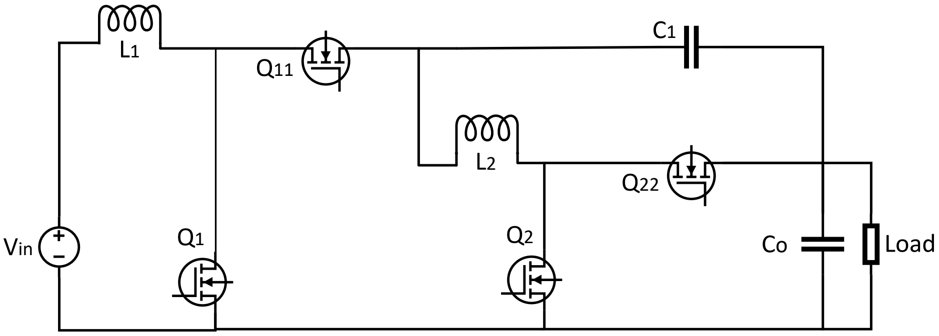

Figure 6.2: Topology of the quadratic gain bi-directional converter.

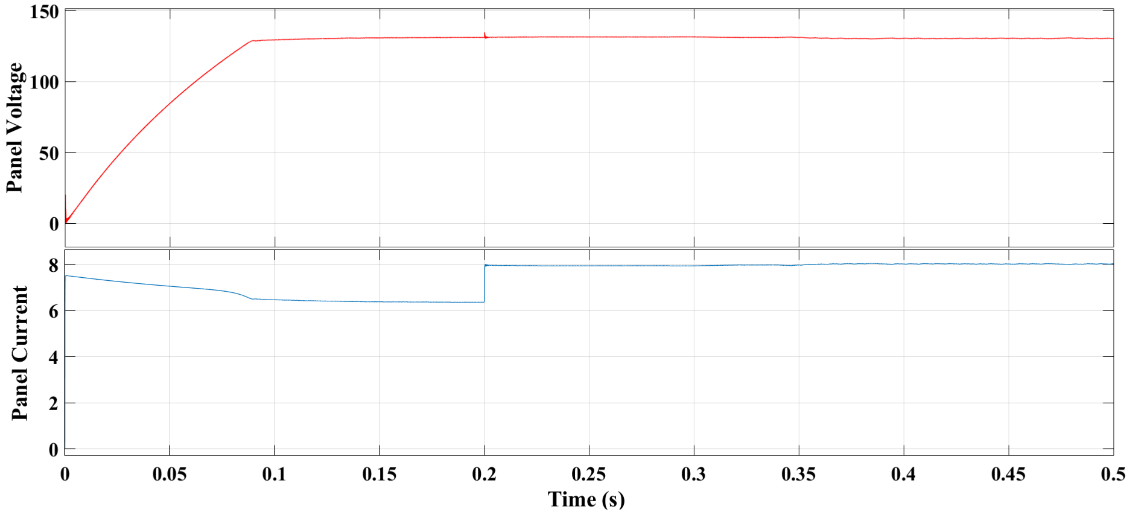

Figure 6.3: PV output with change in irradiance from (800 to 1000 W/m^2) voltage and current.

power generation. The change in operating point entails the change in irradiance to the PV panel from 800 W/m^2 to 1000 W/m^2 at t= 0.2 s. The wind speed is changed at t= 0.3 s from 5m/s to 7 m/s.

The panel voltage and output current of the PV panel is depicted in Figure 6.3. It is observed that there is minimal change in the panel voltage, whereas the operating-current changes from 6.2 A to 8 A at t=0.2, owing to the change in irradiance value. The MPPT technique used here is the INC and is observed to react quickly after the system achieves steady-state. In the region of t=0 s to 0.1 s the DC microgrid was forming, and thus the system was not in a steady-state; thus, the current profile of the PV panel is not smooth. After the DC microgrid has formed at a voltage of 350 V, the MPPT becomes faster.

6.2.2 Wind energy conversion system

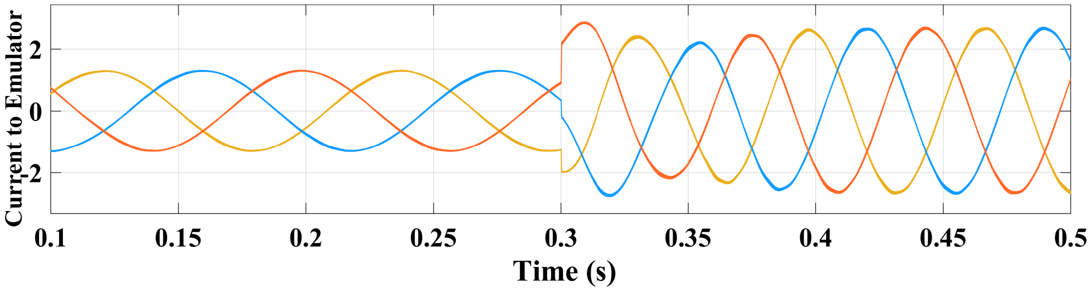

(a) Current of SCIM.

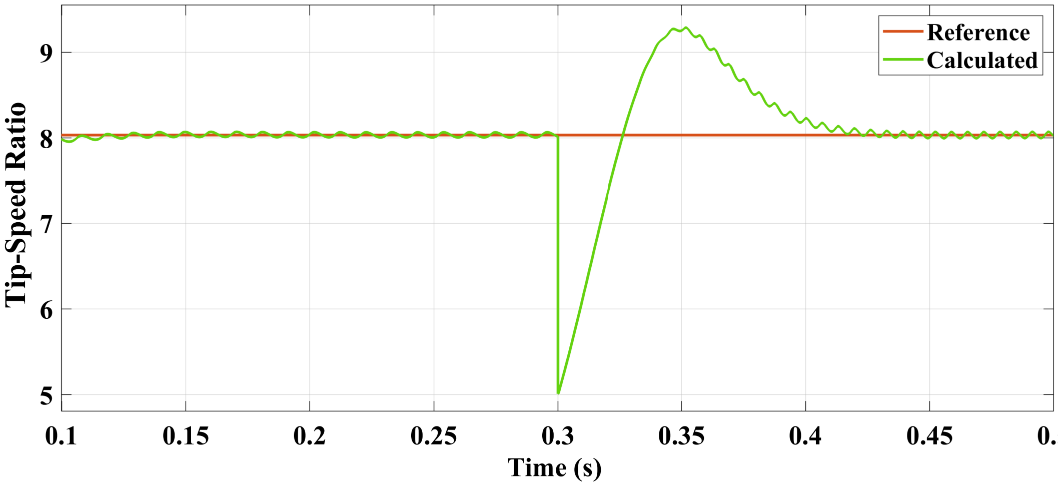

(b) TSR tracking MPPT.

Figure 6.4: Performance of wind turbine emulator and TSR following MPPT.

The performance of the developed wind turbine emulator is presented in Figure 6.4a, Whereas the performance of the TSR-following MPPT technique is depicted in Figure 6.4b. At t = 0.3s the current to the SCIM is observed to increase in response to the change in wind speed command. A sudden drop in the calculated TSR value is observed in Figure 6.4b, as the wind speed is increased abruptly while the rotor speed is still the same; thus, the value of TSR decreases. The controller is kicked into action at this time, and the rotor speed is increased by increasing the developed torque from the SCIM. The recovery of the TSR value is depicted here as well.

The rotor speed and the torque applied on the PMSG are presented in Figure 6.5a. The reaction to the sudden change in the wind speed is shown here. The depiction of how

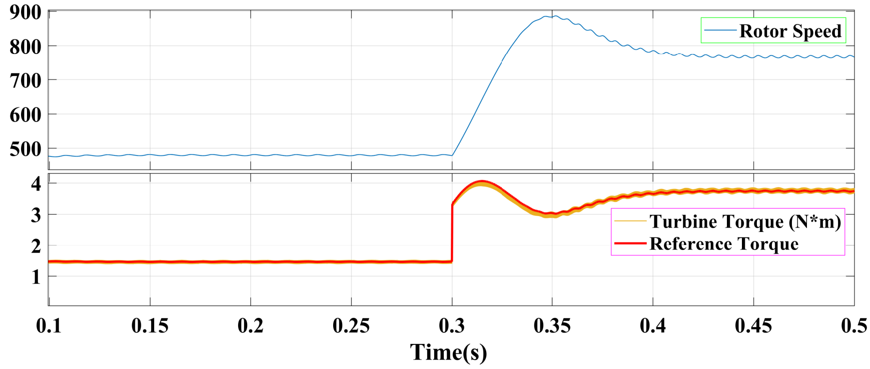

(a) Speed and torque of PMSG.

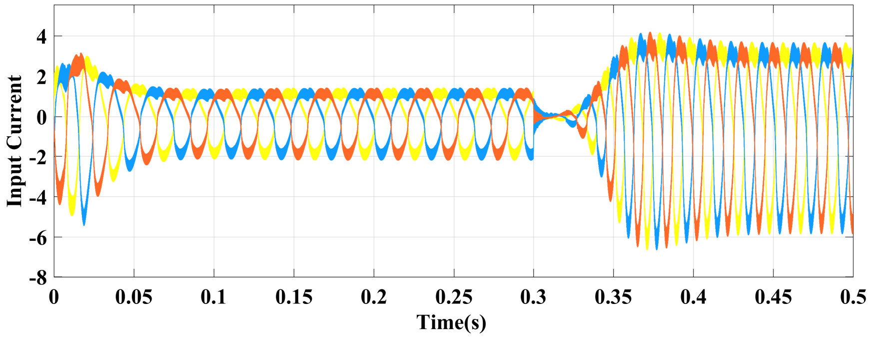

(b) Input current of converter.

Figure 6.5: PMSG characteristics and the input current of the AC to DC converter.

the recovery of the TSR value is happening is evident from these results.

The input current waveform of the three-phase AC to DC converter is shown in Figure 6.5b, at t=0.3 s, the input current is approaching almost zero value, it is due to the fact that the sudden change in the wind speed, drops the TSR value and thus, in turn, the working duty of the converter is decreased to a very low value. The control technique is discussed in detail in section 5.3.2. The total capacitance of a 350 V is more than 22 mF. Thus it absorbs most of the high-frequency harmonics. The input current and the output current correspondingly follow each other, as the output side is designed to work in DICM. It leads to a small ripple in the DC microgrid, which is reflected in the current of the BESS as well. The voltage ripple is of the order of 0.5 V and thus neglected.

6.2.3 DC microgrid control with BESS

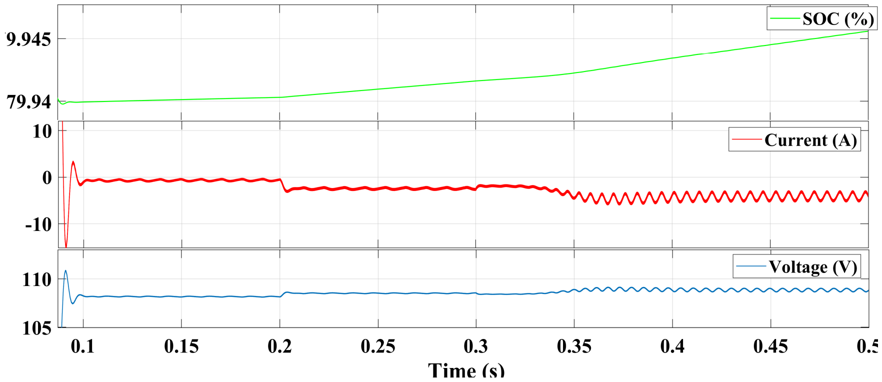

(a) Battery characteristics.

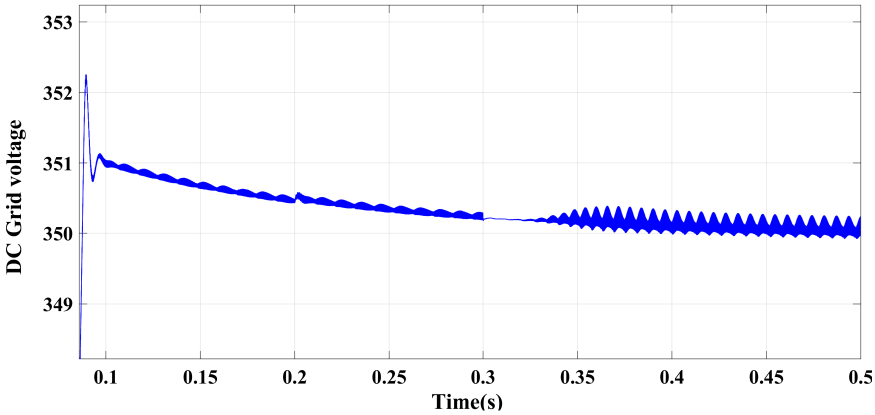

(b) DC microgrid voltage

Figure 6.6: The battery states and formation control of the DC microgrid

The battery characteristics during the control and formation of the DC microgrid are shown in figure 6.6a. It can be observed that at t=0.1, the steady-state is achieved as the current and voltage becomes stable. The SOC of the battery is increasing owing to the fact that the power extracted by load from the DC microgrid is lower than the generated power from the HECS. The DC microgrid voltage is shown in Figure 6.6b. A relatively fast and robust PI controller is used in this case, which enables a low voltage overshoot and stability. The maximum voltage overshoot in the DC microgrid is observed at the starting/formation of the microgrid of 2.2 V. This is a negligible overshoot and follows the IEC 61851-23 standard [121].

6.3 HECS Feeding DC Microgrid with Single-Phase AC Grid

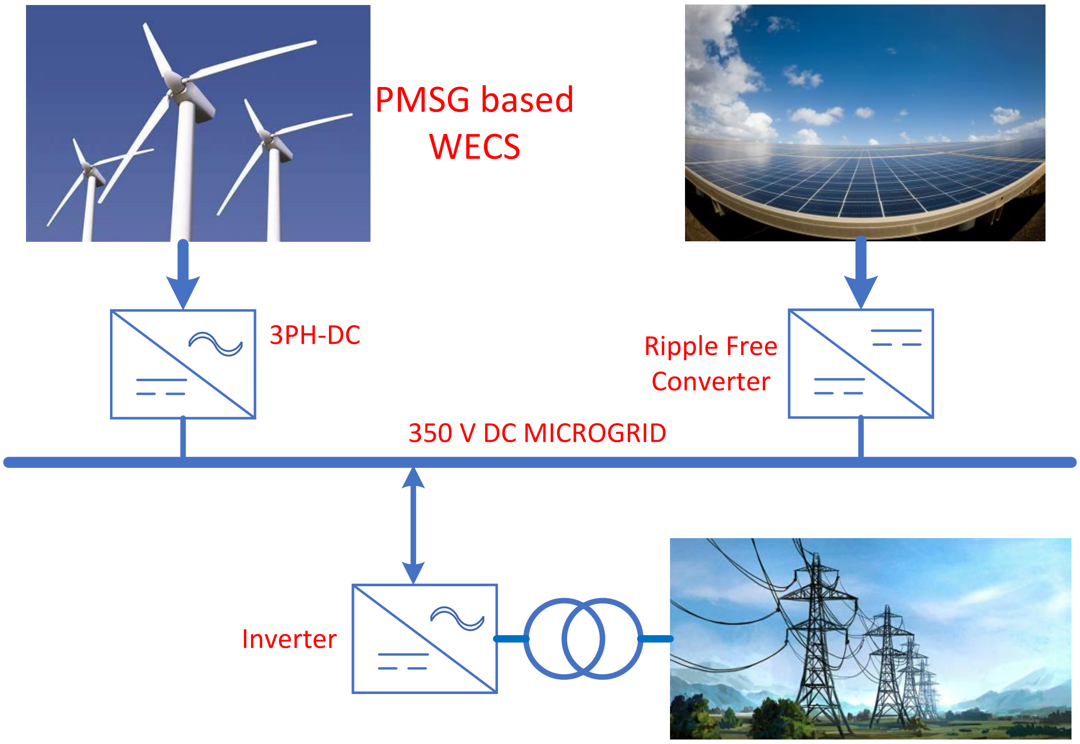

Figure 6.7: Schematic of the system with grid.

Apart from the islanded mode of operation, the DC microgrid can be operated in the grid-connected mode. The schematic diagram of the grid-connected DC microgrid being fed from HECS is shown in Figure 6.7. In place of BESS, the grid can supply the DC microgrid for extended time periods in the absence of solar and wind power sources. Furthermore, the price of the system is cut-off by a large margin as BESS comprises a major part of the installation cost.

For remote and rural areas, the grid connection is not readily available and requires a huge investment in installation of the grid infrastructure. Thus, BESS fed DC microgrids are more preferred in remote locations. Grid connected are more preferred in the urban areas, with stable grid availability. The performance analysis of the solar and wind power generation systems is not done in this section. As they are exactly the same as discussed in Section 6.2.3, the control technique and the performance analysis of the DC microgrid are presented henceforth.

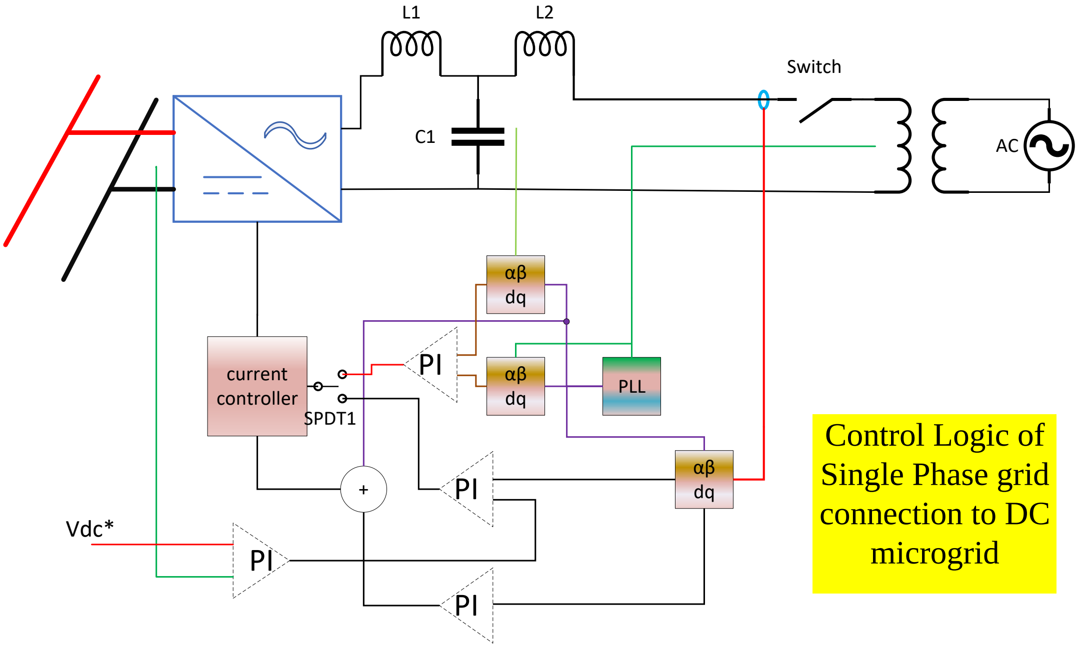

Figure 6.8: Schematics of the control logic of the single-phase inverter.

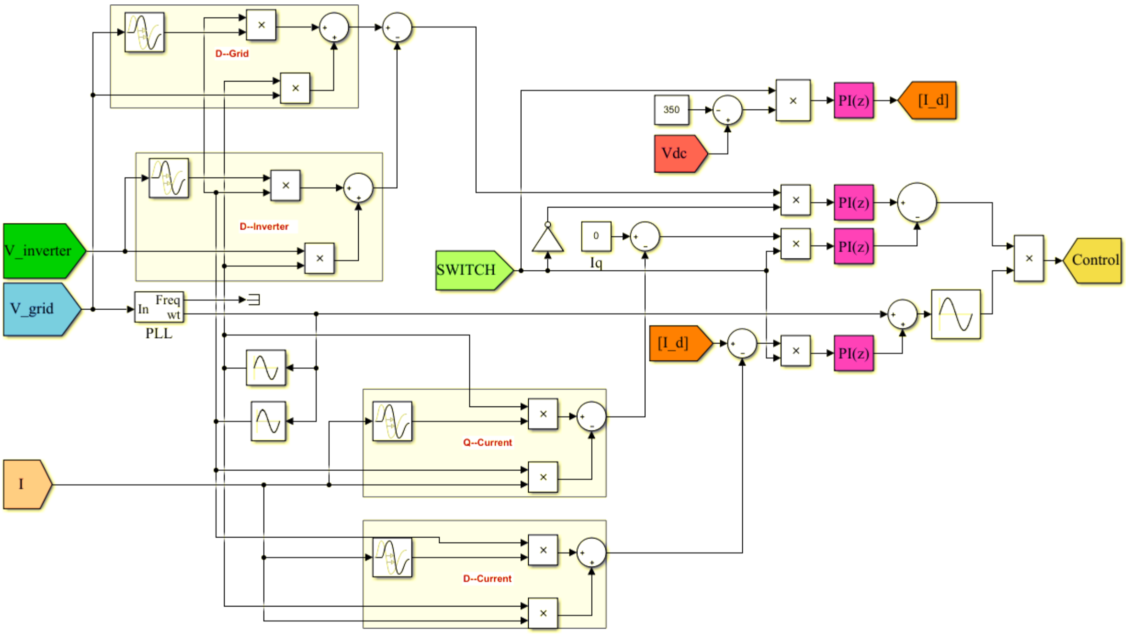

Figure 6.9: Control technique for grid connection and current control.

The control logic of the single-phase inverter is shown in Figure 6.8. The grid voltage is considered here to be a swing bus and thus has constant frequency and voltage. It facilitates the generation of a waveform with a constant 90^circ phase shift from the sensed voltage. This generated waveform having the same amplitude as the sensed voltage leads gives an opportunity to use $\alpha - \beta$ transformation and get the d-q transformation of the grid voltage.

Before connecting the DC microgrid to the single-phase AC grid, the voltages of the grid and filter capacitor C_1 are matched accurately. This matching is performed by using a PI controller to follow the direct-axis component of the grid voltage, as the quadrature-axis component of the voltage is zero. When the voltages are matched, the switch is turned on, and the grid gets connected to the inverter. It generally takes 2-5 cycles for the voltages to be exactly matched, depending on the filter values, switching frequency of the inverter, initialization of the PLL, and DC grid voltage.

After the connection to the grid is made successfully, the control methodology changes from voltage following to current controlling. In this mode of operation, the $\alpha - \beta$ to the d-q transformation of the current is done. The direct axis and quadrature axis values of the current are controlled by using PI controllers. The direct-axis current is controlled by changing the phase of the generated voltage from the inverter, Whereas the quadrature-axis current is controlled by changing the amplitude. The phase is changed by adding a small value generated from the PI controller to the value of the theta(θ) at the generation of modulating signal by d-q to $\alpha - \beta$ transformation. In contrast, the amplitude of the generated voltage is changed by adding the output of the PI controller to the modulation index value generated prior to the grid connection. During this mode of operation, the error to the PI controller, which controls the direct axis value of the voltage before the grid connection is made zero.

The error generated from the reference grid voltage, i.e., 350 V and actual grid voltage, determine the reference of the direct axis current to be fed to the grid. The quadrature axis current is set at zero, but depending on the grid requirement, it can be changed. The voltage of the DC microgrid represents the power generated by the HECS; when the voltage decreases, it means generated power is less than the load demand and vice-versa. As the quadrature axis current cannot control the active power flow, it cannot change the voltage of the DC microgrid. Figure 6.9 presents a detailed description of

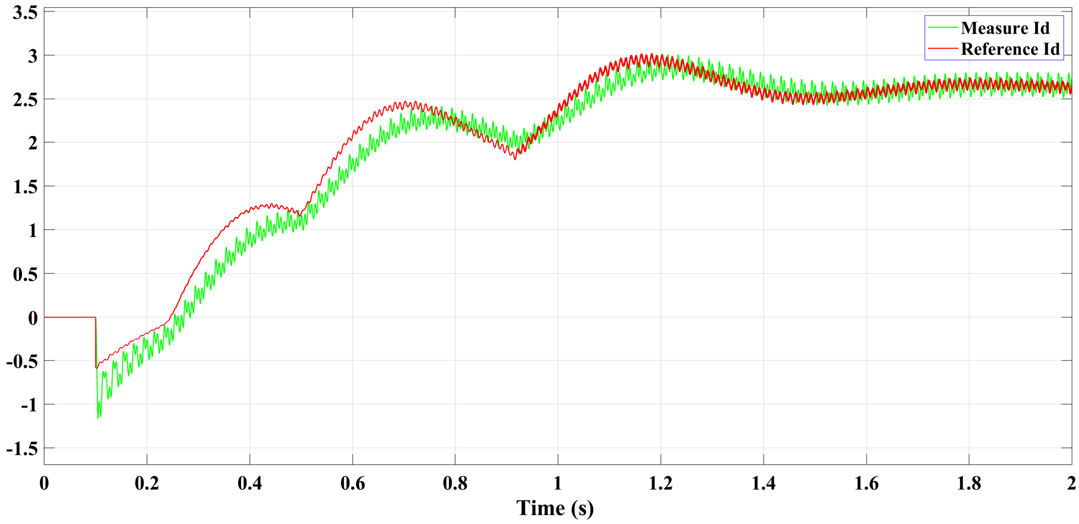

Figure 6.10: The following of the d-axis current with solar irradaince change at t= 0.5 s and wind speed change at t=0.9 s.

control methodology employed in this system.

Figure 6.10 shows the measured(I_d^{meas}) and reference value(I_d^{ref}) of the direct-axis current. Before grid connection (t $<$ 0.1 s), the values of I_d^{meas} and I_d^{ref} are zero. After grid connection, the current control technique kicks into action and tries to make the DC microgrid voltage follow the reference value. Thus, the reference value of current I_d is generated from the PI controller. By controlling the phase shift in the generated voltage with respect to the grid voltage phase, the value direct-axis current is controlled. The effect of the change in solar irradiance at t=0.5 s and change in wind speed at t=0.9 s is evident from the change in the value of the I_d^{ref}, which leads to the corresponding change in the value of I_d^{meas}.

The grid voltage and generated voltage from the inverter are shown in Figure 6.11, which also presents the changes in the grid current. These changes in the grid current values correspond to the changes in the direct-axis current as depicted in Figure 6.10. The direction of current from the grid-side inverter to the grid is deemed to be the positive direction. Thus for power feeding to the grid, the current and grid voltage are in the same phase.

The value of the DC microgrid voltage is presented in Figure 6.12, The corresponding changes due to the solar irradiance change from (800 W/m^3) to (1000 W/m^3) is evident at t=0.5 s. and the wind speed change from 5 m/s to 7 m/s is increasing the microgrid

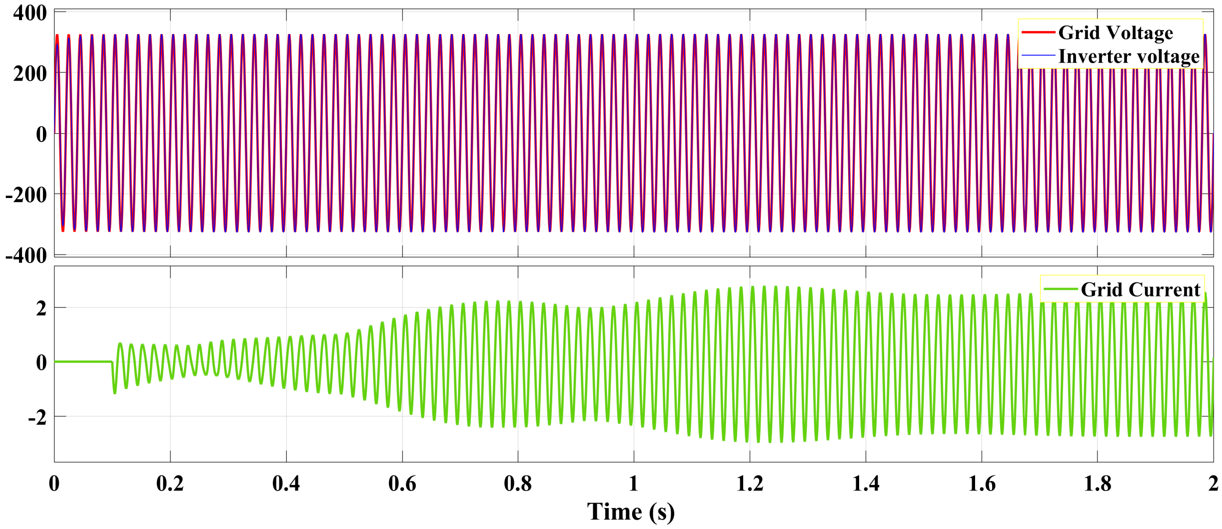

Figure 6.11: Tracking of the grid voltage and change in the grid current.

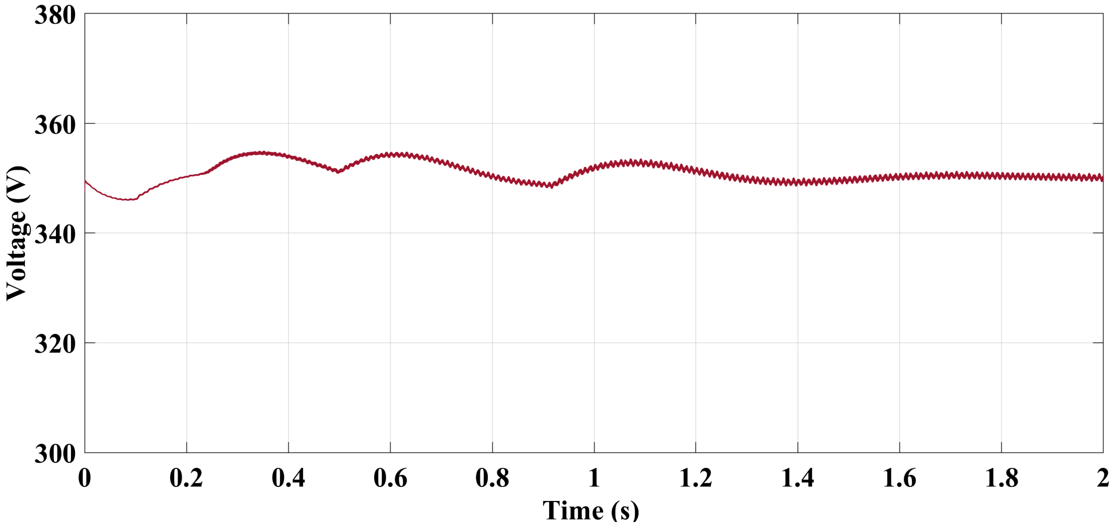

Figure 6.12: DC microgrid voltage regulation.

voltage at t=0.9s. The control of the grid current is feeding the excess power to the grid, thus establishing a power flow balance. This power flow balance is essential for the stable operation of any type of grid.

6.4 Summary

The developments of the HECS using BESS and a Single-phase grid are presented in this chapter. The control techniques and the topologies are explained in detail. The observed results from both systems are presented and discussed. Furthermore, it is observed that the voltage fluctuations in the grid-connected mode are more prominent. As the control of grid current cannot be implemented to be as faster as the current from BESS. Comparing the results presented in Figure 6.6b and Figure 6.12, it is evident that the BESS controlled DC microgrid provides a more stable and fast responding DC microgrid formation. Moreover, the transients in power flow from sudden power changes are mitigated more promptly in the case of the BESS-controlled DC microgrid.

The next chapter presents the conclusive remarks and the future scopes of this thesis.